RSC Advances

ROYAL SOCIETY OF CHEMISTRY

PAPER

View Article Online
View Journal | View Issue

Check for updates

Cite this: *RSC Adv.*, 2026, **16**, 22006

Open Access Article. Published on 27 April 2026. Downloaded on 6/17/2026 5:47:14 PM.
This article is licensed under a Creative Commons Attribution-NonCommercial 3.0 Unported Licence.

Uncovering a stable $Cs_2SnGeCl_6$-lead-free halide double perovskite for photovoltaics through integrated DFT and SCAPS-1D analysis

Hadjer Bendjilali, [ab] Selma Rabhi, *[c] Asadul Islam Shimul,*[d] Shima Sadaf, [e] Sajid Ali Ansari [f] and Mir Waqas Alam*[f]

Received 24th February 2026
Accepted 20th April 2026

DOI: 10.1039/d6ra01612j

rsc.li/rsc-advances

Eco-friendly halide perovskites have garnered interest as viable options for next-generation optoelectronic and solar-energy technologies due to their adjustable bandgaps, robust light absorption, and excellent charge-transport properties. This study presents the inaugural comprehensive theoretical examination of the eco-friendly double perovskite '$Cs_2SnGeCl_6$' through two methodologies: density functional theory (DFT) for elucidating the physical properties of this compound and SCAPS-1D simulations to assess its viability as an absorber layer in perovskite solar cells (PSCs). Using the advanced calculation functions in DFT, we confirm that $Cs_2SnGeCl_6$ is stable in terms of structure, mechanical stability, and thermodynamics, making it a good choice for solar energy harvesting. This stability is enhanced by positive phonon dispersion, a direct bandgap of around 1.837 eV derived by the application of TB-mBJ, a robust computational method characterized by significant absorption over the visible spectrum, and advantageous optical conductivity. Building on these electronic and optical insights, SCAPS-1D simulations were performed using DFT-derived parameters to model sixteen n–i–p device architectures incorporating newly engineered electron and hole transport layers. The best initial configuration, FTO/SnS_2/$Cs_2SnGeCl_6$/$CuGaO_2$ yielded a power conversion efficiency (PCE) of 20.31%, and after optimization, the PCE increased to 23.29%.

1. Introduction

The imperative need to mitigate climate change and the increasing global energy consumption have underscored the importance of the pursuit of sustainable and renewable energy sources.[1] Due to its abundance and environmental benefits, solar energy is considered one of the most promising alternatives. Metal halide perovskites have garnered considerable interest in photovoltaic research in recent years due to their remarkable optoelectronic characteristics, including adjustable band gaps, elevated absorption coefficients, extended carrier diffusion lengths, and solution-processable manufacturing methods.[2–4] These characteristics have allowed perovskite solar cells (PSCs) to attain exceptional power conversion efficiencies (PCEs) above 26.95%,[5] competing with or exceeding those of conventional technologies like silicon-based photovoltaics. The intrinsic issues associated with conventional lead halide perovskites, including environmental toxicity and long-term stability concerns, hinder their widespread commercialization.[6–9] Significant research endeavors have concentrated on lead-free halide perovskites and double perovskite derivatives to mitigate these problems, providing enhanced chemical stability and diminished toxicity while preserving favorable optoelectronic properties. In this context, double perovskites have lately emerged as viable alternatives, with DFT simulations indicating that these compounds possess direct band gaps ranging from 1.6 to 2.1 eV, rendering them suitable for visible-light absorption.[10–12] Their potential for optoelectronic applications, particularly in solar energy harvesting, is underscored by their favorable refractive indices, absorption coefficients, and dielectric responses. Recent studies indicate that $Cs_2AgBiBr_6$ is a viable alternative to novel lead-based perovskites for solar cell applications,[13,14] these compounds exhibit exceptional photovoltaic performance and are subjected to additional experimental investigation.

---

[a] *Dielectric Materials and Polymers Team, Laboratory of Materials Physics, Faculty of Physics, University of Science and Technology Houari Boumediene USTHB, BP No 32, El Alia 16111, Algiers, Algeria*

[b] *Condensed Matter and Sustainable Development Laboratory (LMCDD), University of Sidi Bel-Abbes, Sidi Bel-Abbes 22000, Algeria*

[c] *Laboratory of Innovative Environmental Preservation Techniques, Mechanical Engineering Department, Constantine 1 University, 25000 Constantine, Algeria. E-mail: selma.rabhi@umc.edu.dz*

[d] *Department of Electrical and Electronic Engineering, Gopalganj Science and Technology University, Gopalganj-8100, Bangladesh. E-mail: shimul.18eee009@gstu.edu.bd*

[e] *Department of Electrical Engineering, College of Engineering King Faisal University, Al-Ahsa 31982, Saudi Arabia*

[f] *Department of Physics, College of Science, King Faisal University, Al-Ahsa 31982, Saudi Arabia. E-mail: wmir@kfu.edu.sa*

© 2026 The Author(s). Published by the Royal Society of Chemistry

Open Access Article. Published on 27 April 2026. Downloaded on 6/17/2026 5:47:14 PM.
This article is licensed under a Creative Commons Attribution-NonCommercial 3.0 Unported Licence.

Table 1 Inputs for SCAPS-1D for all layers

	TCO	PVK			HTLs			ETLs		
Parameters	FTO	$Cs_2SnGeCl_6$	$CuGaO_2$	CuI	CBTS	D-PBTTT-14	SnS_2	MZO	LBSO	Nb_2O_5
Thickness (nm)	100	500	100	100	100	100	100		100	100
E_g (eV)	3.50	1.837	2.51	3.4	1.5	2.16	1.850	3.35	3.12	3.4
χ (eV)	4.00	4.12	3.10	2.1	4.22	3.2	4.26	4	4.4	3.9
ε_r	9	3.73	3.0	10	5.5	10	17.7	66	22	10
N_c (cm^{-3})	2.2×10^{18}	1.95×10^{18}	1.0×10^{19}	2×10^{19}	2.20×10^{18}	2.8×10^{19}	7.32×10^{18}	1×10^{19}	1.8×10^{20}	2.20×10^{18}
N_v (cm^{-3})	2.2×10^{18}	1.76×10^{19}	1.0×10^{19}	1.8×10^{19}	1.80×10^{19}	1.0×10^{19}	1×10^{19}	1×10^{19}	1.8×10^{20}	1.8×10^{19}
μ_n ($cm^2 V^{-1} s^{-1}$)	20	18.32	0.2	12	5.00	2.83×10^{-3}	50	0.05	6.9×10^{-1}	20
μ_p ($cm^2 V^{-1} s^{-1}$)	10	3.55	0.2	28	1.50	2.83×10^{-3}	25	0.05	6.9×10^{-1}	0.1
N_D (cm^{-3})	1.0×10^{15}	0	0	0	0	0	9.85×10^{19}	1×10^{17}	2×10^{21}	1.00×10^{16}
N_A (cm^{-3})	0	0	1.0×10^{18}	2×10^{19}	1.00×10^{18}	1×10^{18}	0	0	0	0
N_t (cm^{-3})	Varied	Varied	1.0×10^{15}	1.0×10^{15}	1.00×10^{14}	1×10^{14}	1×10^{14}	1×10^{14}	1.0×10^{14}	1.00×10^{15}
Reference	25	DFT	26	27	28	29	27	30	31	32

Although halide double perovskites (HDPs) such as cesium-based compounds including $Cs_2NaBiBr_6$, $Cs_2InBiBr_6$, $Cs_2AgBiBr_6$, $KBaTeBiO_6$, and $Cs_2CuBiBr_6$ have demonstrated potential efficiencies for solar energy conversion, there are still a limited number of experimental investigations.[15,16] This study examines the chlorine analogue $Cs_2SnGeCl_6$ for the first time, driven by their favorable electrical and optical characteristics that render them suitable for solar applications. To fully harness the potential of these chemicals in solar energy harvesting, it is essential to integrate first-principles predictions with device-level models. Density Functional Theory (DFT) facilitates the examination of essential structural, electrical, and optical properties, whereas numerical simulations of SCAPS-1D enable the analysis of charge transport, recombination mechanisms, and layer optimization within comprehensive device topologies. This integrated methodology enhances the comprehension of $Cs_2SnGeCl_6$ perovskites while expediting their incorporation into commercial solar technology.

2. Computational details

In this work, all first-principles density functional theory (DFT) calculations for the chloro-perovskite compound $Cs_2SnGeCl_6$ were achieved using the full-potential linearized augmented plane wave (FP-LAPW) method,[17] implemented in the Wien2k code.[18] The generalized gradient approximation to the Perdew–Burke–Ernzerhof functional (GGA-PBE) is used to represent the electron–electron exchange–correlation interaction energy and to calculate the ground-state properties.[19] In addition, the following expression describes the Tran–Blaha modified Becke–Johnson (TB-mBJ) potential,[20] renowned for its accurate calculation of semiconductor band gaps: $V^{\mathrm{mBJ}}_{(x,\sigma)}(r) = cV^{\mathrm{BR}}_{(x,\sigma)}(r) + (3c-2)\frac{1}{\pi}\frac{\sqrt{5}}{12}\frac{\sqrt{2t_\sigma(r)}}{\rho_\sigma(r)}$ where, c, $\rho_\sigma(r)$ and $t_\sigma(r)$ denotes the charge convergence factor, the density of states and the kinetic energy, respectively. The c factor is calculated using the following relation: $c = \alpha + \left(\beta \frac{1}{V_{\mathrm{cell}}} \int d^3(r) \frac{|\nabla \rho(r)|}{\rho(r)}\right)^{1/2}$, α and β are arbitrary constants, whose values are adjusted in Wien2K to obtain the precise electronic band structure.[21] The Monkhorst–Pack method was used for Brillouin zone integration with a 13 × 13 × 13 k-cell to calculate the electronic structure.[22] The charge convergence threshold is set to $10^{-4}|e|$ Ry for self-consistency iterations, with e representing the electron charge. Optical properties are determined using 2000 k-points. In non-overlapping muffin spheres, the wave functions are extended up to an angular momentum quantum number $l_{\max} = 10$ using spherical harmonics. A cutoff energy of −6.0 Ry is applied to differentiate core states from valence states. The charge density is expanded in Fourier series up to a maximum reciprocal space vector norm of $G_{\max} = 12\ (\mathrm{a.u.})^{-1}$. For interstitial regions, a plane-wave basis set is used with a cutoff parameter $K_{\max} = 7/R_{\mathrm{MT}}$, where R_{MT} is the smallest muffin-tin radius and $K_{\max}$ is the maximum K vector in the first Brillouin zone. Moreover, we evaluated the photovoltaic performance of $Cs_2SnGeCl_6$-based PSCs by modelling and simulating the using the DFT derived parameters of $Cs_2SnGeCl_6$. Prior to the experimental fabrication of these materials into solar cell devices, the simulation phase, which is conducted using SCAPS-1D, is essential for the purpose of conserving both time and resources. The distribution and transport of charge carriers within the device are collectively described by these equations, which facilitate the precise prediction of its electrical behavior and efficacy.[23]

$$\frac{\partial}{\partial x}\left(-\varepsilon(x)\frac{\partial V}{\partial x}\right) = q[p(x) - n(x) + N_D{}^{+}(x) - N_A{}^{-}(x) + p_t(x) - n_t(x)] \tag{1}$$

$$\frac{\partial n}{\partial t} = \frac{1}{q}\frac{\partial J_n}{\partial x} + G_n - R_n \tag{2}$$

$$\frac{\partial p}{\partial t} = -\frac{1}{q}\frac{\partial J_p}{\partial x} + G_p - R_p \tag{3}$$

where: ε, V, q, $p(x)$, $n(x)$, $N_D{}^{+}(x)$, $N_A{}^{-}(x)$, $p_t(x)$, and $n_t(x)$ are dielectric permittivity, electric potential, electronic charge, free hole density, free electron density, donor density, acceptor

Open Access Article. Published on 27 April 2026. Downloaded on 6/17/2026 5:47:14 PM.
This article is licensed under a Creative Commons Attribution-NonCommercial 3.0 Unported Licence.

density, trap density of holes, and trap density of electrons, respectively. These equations are solved by the program to analyze basic properties. Standard solar cell testing parameters, including a temperature of 300 K. The computations were conducted at a temperature of 300 K and an integrated power density of 1000 W m^{-2} (AM1.5G).[24] The extracted parameters from DFT and literature used in the modeling and simulation with SCAPS-1D are enlisted in Table 1.

3. Results and discussion

3.1 Probing the stability of $Cs_2SnGeCl_6$ double halide perovskites

An exhaustive analysis of the structural, thermodynamic, and mechanical properties of materials like $Cs_2SnGeCl_6$ are essential to ascertain their stability. Initially, we commenced with the structural analysis, which reveals a direct correlation between the lattice constants of the compounds and the measurements of their ionic radii where are listed on Table 2. The crystal structure with space group $Fm\bar{3}m$ (#225) of $Cs_2SnGeCl_6$ compound is generated with optimized lattice constants as presented in the inset of Fig. 1. In the unit cell structures of the materials given, the Wyckoff coordinates of Cs are (0.25, 0.25, 0.25), Sn are (0.5, 0.5, 0.5), Ge are (0, 0, 0), and for Cl, they are (0, 0, 0.23). Based on the lattice parameters found in the literature, we did a full optimization to find the most stable crystallographic structure of $Cs_2SnGeCl_6$. Fig. 1 shows the total energy *versus* volume curves that were made using the PBE-GGA functional in the WIEN2k code. Next, the Murnaghan equation of state was used to find the equilibrium volume that gives the least amount of total energy. This method not only found the best lattice constants and unit-cell volume, but it also found important structural parameters like the bulk modulus (B) and the ground-state energy (E_0).[33]

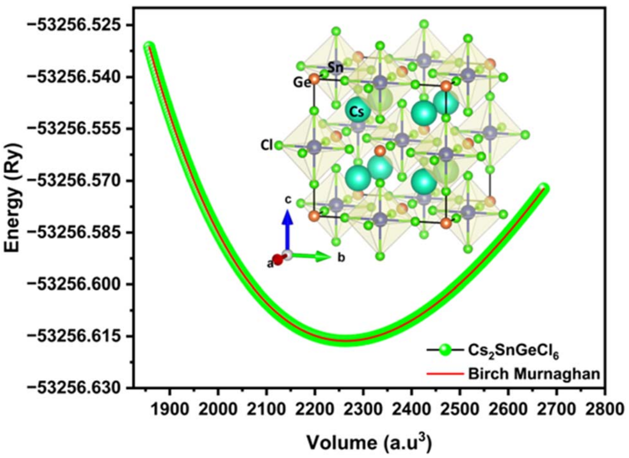

Fig. 1 Total energy with Birch–Murnaghan-fitted optimum energy curves *versus* volume for the double perovskite $Cs_2SnGeCl_6$, with the inset presented the 3D structure of $Cs_2SnGeCl_6$.

Table 2 Ionic radii, and Mulliken electronegativity of the constituent atoms in $Cs_2SnGeCl_6$ halide double perovskites

Atoms	Ionic radii (Å)	Mulliken electronegativity (eV)
Cs	1.74	2.183
Sn	0.69	4.228
Ge	0.53	4.565
1.81	0.44	8.292

As shown in Table 3, the optimized structural parameters obtained in this work for $Cs_2SnGeCl_6$ show good agreement with previously reported data.[34,35] Our calculated lattice constant of $a = b = c = 11.030$ Å is very close to the value of 10.994 Å reported in Dahane *et al.*,[34] with a deviation of less than 0.3%. The ground-state volume ($V_0 = 2263.770$ Å^3) is also consistent, which shows that our structural optimization is reliable. The fact that our computational method is more accurate is shown by how well the lattice parameters and geometric descriptors agree with the literature. In contrast, the structure reported in the work of Bharath *et al.* adopts a lower-symmetry description with $a = c = 5.504$ Å and $b = 10.951$ Å ($V_0 = 331.720$ Å^3),[35] which corresponds to a reduced or primitive cell. This difference arises from the choice of the crystallographic setting rather than a discrepancy in the material itself. For halide perovskites, the Goldschmidt tolerance factor (τ) provides a first indication of structural stability. Values between 0.8 and 1.0 generally correspond to a cubic phase, whereas $\tau < 0.8$ favors orthorhombic distortions, and $\tau > 1$ typically leads to hexagonal structures.[36] A τ value close to 1 suggests that the lattice can accommodate the constituent ions with minimal deformation.[37] For a perovskite to sustain an ideal cubic configuration, μ should be greater than 0.41. The Goldschmidt tolerance factor (τ) and the octahedral factor (μ) obtained using eqn (4).[38] The calculated stability descriptors indicate that the tolerance factor ($\tau = 0.9437$) and octahedral factor ($\mu = 0.5276$) fall within the ideal range for cubic halide perovskites. These values are in close agreement with previously reported data ($\tau = 0.926$ and $\mu = 0.527$), the slight deviation in τ may be attributed to differences in the choice of ionic radii or computational methodology.

$$\tau = \frac{(r_A + r_X)}{\sqrt{2}(r_B + r_X)} \text{ and } \mu = \frac{r_B}{r_X} \tag{4}$$

Furthermore, the formation energy (E_f) obtained in this study (−2.3465 eV per atom) obtained by eqn (5), the E_f of our compound is significantly lower (more negative) than the value of −1.3187 eV per atom reported in Dahane *et al.*,[34] indicating a higher thermodynamic stability in our optimized configuration.

$$E_f = \frac{E_{tot}^{Cs_2SnGeCl_6} - \left(2E_{Cs}^{Bulk} + E_{Sn}^{Bulk} + E_{Ge}^{Bulk} + 6E_{Cl}^{Bulk}\right)}{10} \tag{5}$$

$E_{tot}^{Cs_2SnGeCl_6}$ refers to the total energy of the compound $Cs_2SnGeCl_6$, while E_{Cs}^{Bulk}, E_{Sn}^{Bulk}, E_{Ge}^{Bulk} and E_{Cl}^{Bulk} reflect the individual energies of atoms.

In addition, phonon dispersion calculations offer critical insight into the dynamic stability of crystalline materials and

© 2026 The Author(s). Published by the Royal Society of Chemistry

Open Access Article. Published on 27 April 2026. Downloaded on 6/17/2026 5:47:14 PM.
This article is licensed under a Creative Commons Attribution-NonCommercial 3.0 Unported Licence.

Table 3 The calculated optimal structural parameters, formation energy (E_f), and Goldschmidt factors (τ and μ) of the $Cs_2SnGeCl_6$ compound, compared with literature data

Structural parameters	Lattice constant (Å) $a = b = c$	Volume at ground state (V_0)	Ground state energy (E_0) (Ry)	Tolerance factor (τ)	Octahedral factor (μ)	Formation energy (E_f) (eV per atom)
$Cs_2SnGeCl_6$	11.0297	2263.7692	−53256.616325	0.9437	0.5276	−2.346514
$Cs_2SnGeCl_6$ (ref. 34)	10.994	2241.824	—	0.926	0.527	−1.3187
$Cs_2SnGeCl_6$ (ref. 35)	$a = c = 5.504$ $b = 10.951$	331.72	—	—	—	—

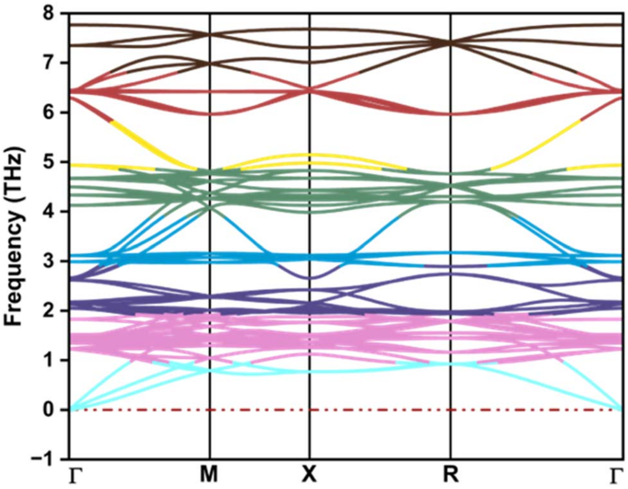

Fig. 2 Frequency-energy dependence while using phonon calculations for the $Cs_2SnGeCl_6$ compound.

are reported here for the first time for $Cs_2SnGeCl_6$. Fig. 2 illustrates the phonon dispersion curve, computed along the high-symmetry directions of the Brillouin zone for the unit cell. Dynamically stable materials are characterized by real (positive) phonon frequencies, whereas the presence of imaginary (negative) frequencies indicates structural instability.[39] The phonon spectrum obtained for $Cs_2SnGeCl_6$ includes only real frequencies, confirming the absence of soft modes and validating its dynamic stability. These stable phonon branches arise from collective lattice vibrations and long-wavelength atomic motions, which ensure well-defined lattice dynamics and further reinforce the structural robustness of the material.[40]

To obtain a more accurate understanding of the mechanical stability and behavior of $Cs_2SnGeCl_6$, we investigated its elastic properties, which are essential for guiding the development of advanced functional materials. The elastic constants (C_{ij}) were calculated using the IRelast package integrated within WIEN2k, which is well-suited for cubic crystal systems.[41] According to the Chapin approach, only three independent elastic constants are required for cubic symmetry: C_{11}, C_{12}, and C_{44}. In this framework, C_{11} represents resistance to uniaxial compression, while C_{12} describes the coupling between stresses and strains along orthogonal directions.[42] As expected, C_{11} (54.08 GPa) as found to be higher than C_{12} (10.47 GPa), indicates strong resistance to longitudinal compression. The relatively low value of C_{44} suggests that the lattice exhibits shear flexibility, which may be attributed to the inherent softness and reduced rigidity of the chloride sublattice,[43] and this behavior is typical for halide perovskites with flexible metal-halide frameworks. Moreover, the computed elastic constants fulfill Huang–Born theory's mechanical stability criteria for cubic,[44] $(C_{11} - C_{12}) > 0$, $C_{44} > 0$, $(C_{11} + 2C_{12}) > 0$, and $C_{11} > B > C_{12} > 0$ confirming that $Cs_2SnGeCl_6$ is mechanically stable in its optimized phase (see Table 4). Furthermore, two fundamental parameters that describe the mechanical behavior of $Cs_2SnGeCl_6$ are the bulk modulus and the shear modulus. The calculated bulk modulus ($B_H = 25.01$ GPa) reflects a moderate resistance to volume compression, indicating that the material can withstand hydrostatic pressure without undergoing structural collapse. In contrast, the relatively low shear modulus ($G_H = 13.75$ GPa) suggests limited resistance to shape deformation, which aligns with the intrinsic softness of the chloride-based sublattice and contributes to the overall mechanical flexibility of the structure. The moduli are ascertained utilizing the Hill approximation:[6]

$$B_H = B_V = B_R = (C_{11} + 2C_{12})/3 \text{ and } G = G_H = (G_V + G_R)/2 \quad (6)$$

where, the shear modulus G_V and G_R can be approximated according to Voigt and Reuss:[42]

$$G_V = (C_{11} - C_{12} + 3C_{44})/5 \text{ and } G_R = \frac{5C_{44}(C_{11} - C_{12})}{4C_{44} + 3(C_{11} - C_{12})} \quad (7)$$

The ratio between these two moduli provides further insight into the material's ductility. The Pugh's ratio ($B_H/G_H = 1.82$) slightly exceeds the commonly accepted ductile–brittle threshold of 1.75, classifying $Cs_2SnGeCl_6$ as ductile rather than brittle.[45] This mechanical character implies a higher tolerance

Table 4 Elastic constants and derived mechanical properties of $Cs_2SnGeCl_6$

Compounds	C_{11} (GPa)	C_{12} (GPa)	C_{44} (GPa)	B_H (GPa)	A	G_H	E_H (GPa)	V_H	B_H/G_H	T_m (K)
$Cs_2SnGeCl_6$	54.08	10.47	10.01	25.01	0.46	13.75	34.86	0.267	1.81	872.60

Open Access Article. Published on 27 April 2026. Downloaded on 6/17/2026 5:47:14 PM.
This article is licensed under a Creative Commons Attribution-NonCommercial 3.0 Unported Licence.

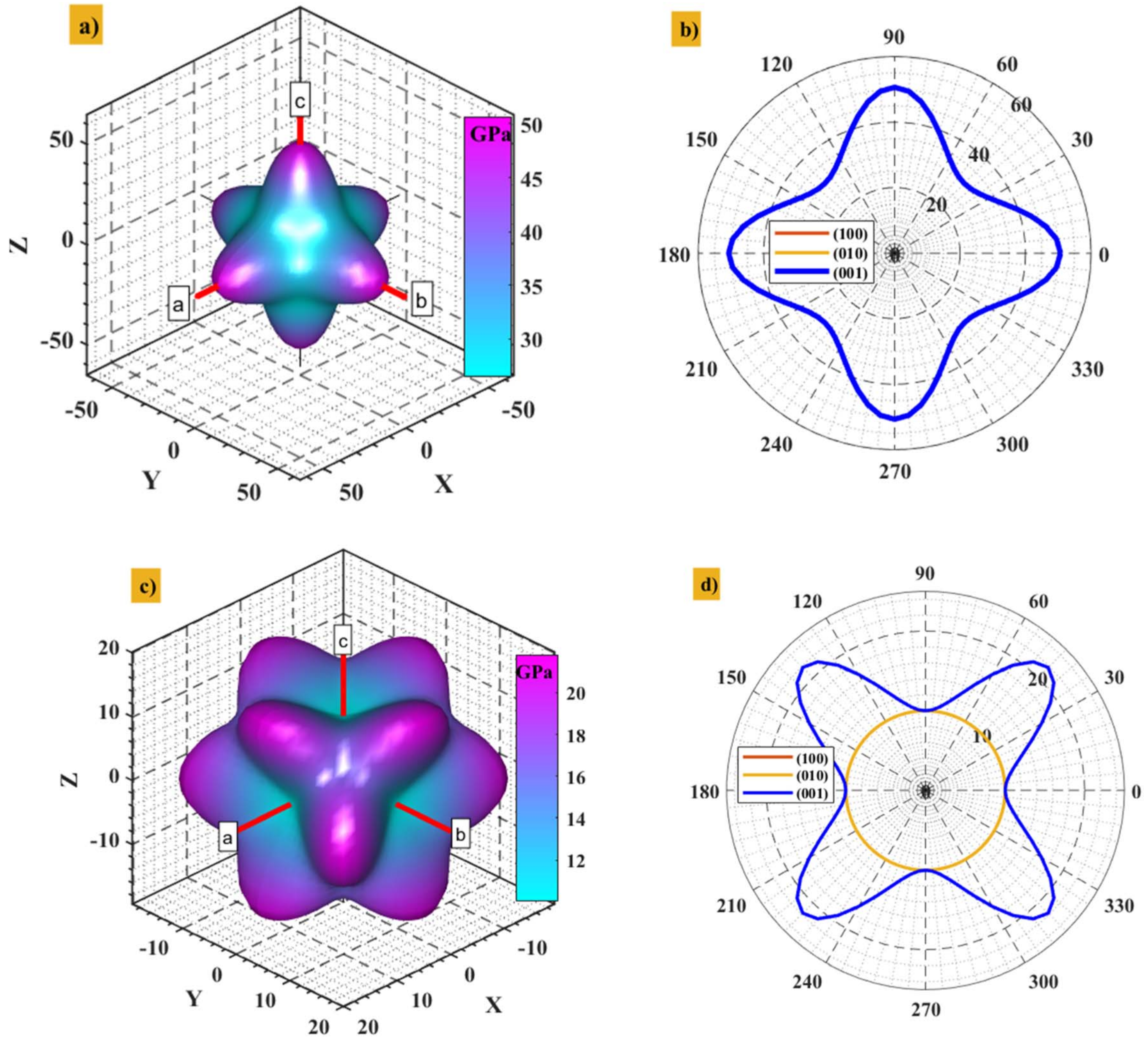

Fig. 3 (a) The 3D and (b) 2D projections of Young's modulus, and (c) 3D and (d) 2D shear modulus of the double perovskite $Cs_2SnGeCl_6$.

to stress and enhances its suitability for thin-film fabrication and flexible device applications.[46] In addition to the bulk and shear moduli, the Young's modulus ($E_H = 34.86$ GPa) provides further insight into the elastic response of $Cs_2SnGeCl_6$. This value is calculated by using eqn (8), E_H indicates moderate stiffness, meaning the material can elastically deform under

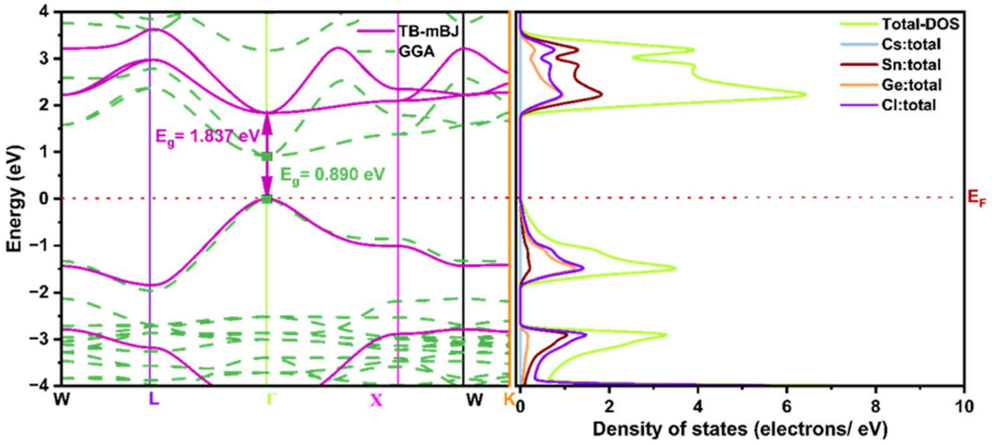

Fig. 4 Band structure and the total density of states of the double perovskite $Cs_2SnGeCl_6$ using GGA and TB-mBJ approximations.

Open Access Article. Published on 27 April 2026. Downloaded on 6/17/2026 5:47:14 PM.
This article is licensed under a Creative Commons Attribution-NonCommercial 3.0 Unported Licence.

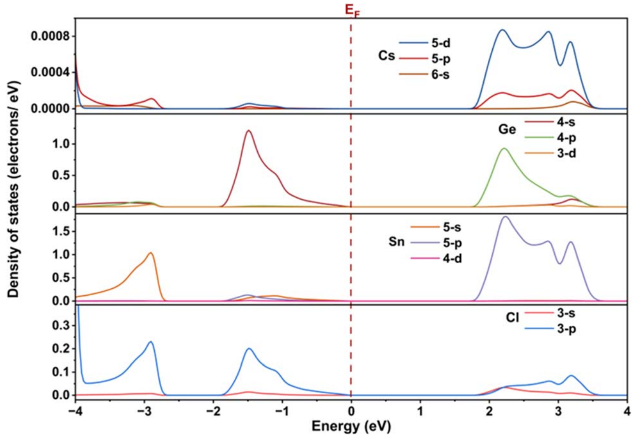

Fig. 5 Partial densities of electronic states of the $Cs_2SnGeCl_6$ compound using TB-mBJ potential.

applied stress and return to its original shape without fracturing. Compared to other halide perovskites, this modulus places $Cs_2SnGeCl_6$ in a mechanically flexible regime rather than a rigid or brittle one. Such an intermediate Young's modulus is advantageous for integrating the material into flexible or layered optoelectronic devices, making it a promising candidate for thin-film photovoltaics, wearable electronics, and deformable energy devices where tolerance to bending, strain, and mechanical handling is required.

$$E_H = 9B_HG_H/(3B_H + G_H) \tag{8}$$

Furthermore, the Poisson's ratio ($\nu_H = 0.267$) further supports the ductile nature of $Cs_2SnGeCl_6$, as it falls within the typical range for ductile crystalline solids (0.25–0.35). A value in this interval indicates that the material can undergo lateral expansion when compressed and sustain deformation without fracturing. This degree of ductility is particularly beneficial for flexible perovskite solar cell fabrication and long-term device stability, where mechanical flexibility and resistance to crack formation are essential. Moreover, the estimated melting temperature ($T_m = 872.60$ K) shows that the compound is thermodynamically stable and that it can handle heat well enough for use in optoelectronics. This temperature is approximated by:[47]

$$T_m = 553 + 5.19C_{11} \pm 300 \tag{9}$$

Finally, the directional dependence of the mechanical behavior of $Cs_2SnGeCl_6$ can be assessed using Zener's anisotropy factor (A), which differentiates isotropic materials ($A = 1$) from anisotropic ones.[48] The calculated value of $A = 0.459$ indicates moderate elastic anisotropy, meaning that the material's mechanical response varies with crystallographic direction. Such anisotropy is common in halide perovskites and may influence properties like crack propagation, cleavage planes, and strain accommodation in thin-film or device architectures. The anisotropy of $Cs_2SnGeCl_6$ was further examined through the 2D and 3D projections of Young's modulus, shear modulus, and Poisson's ratio, which reveal how the elastic response varies with crystallographic direction. The 3D surface of Young's modulus (see Fig. 3(a)) displays a lobed structure deviating from spherical symmetry, indicating that stiffness is direction-dependent, with higher values (50 GPa) observed along ⟨100⟩ direction and lower values along others, consistent with the moderate elastic anisotropy inferred from Zener's factor. The corresponding 2D polar plots reinforce this behavior by showing noticeable variation across different crystallographic planes, rather than a perfect circular contour expected for isotropic systems (see Fig. 3(a)). Similarly, in Fig. 3(c) and (d) the 3D and 2D projections of the shear modulus show a non-spherical distribution, confirming that resistance to shear deformation is not uniform throughout the lattice, which aligns with the influence of the softer chloride-based framework. However, a circular trace observed for the (010) plane indicates nearly isotropic shear resistance within that orientation, suggesting uniform deformation response in that crystallographic direction. The (100) and (001) projection follow a similar trend, further reinforcing that shear deformation does not occur uniformly across all planes. Overall, the mechanical indicators show that $Cs_2SnGeCl_6$ has ductility, moderate stiffness, elastic anisotropy, and structural stability. These are all good qualities for photovoltaic and energy-related applications where thermal and mechanical reliability are important.

3.2 Probing the electronic properties of $Cs_2SnGeCl_6$ double halide perovskites

Understanding the electronic properties of halide perovskites is essential for evaluating their suitability in optoelectronic and photovoltaic devices. Parameters such as the bandgap nature, dispersion of the electronic bands, and the orbital contributions near the Fermi level directly influence charge transport, light absorption, and recombination dynamics. In $Cs_2SnGeCl_6$, probing the electronic structure through first-principles calculations offers valuable insight into how the cation sublattice and halide coordination shape the material's semiconducting behavior. The band structure was calculated using two different exchange–correlation functionals as presented in Fig. 4. The PBE-GGA approach yields a direct bandgap of 0.880 eV (Γ), which is consistent with the well-known tendency of generalized gradient approximations to underestimate the energy gap

Table 5 Summary of electronic calculated parameters

	E_g (eV) with GGA/TB-mBJ	m_e^*	m_h^*	N_C (cm^{-3})	N_V (cm^{-3})	μ_e (cm^2 V^{-1} s^{-1})	μ_h (cm^2 V^{-1} s^{-1})
$Cs_2SnGeCl_6$	0.890/1.837	4.956	0.960	2.769×10^{20}	2.359×10^{19}	3.547	18.323

© 2026 The Author(s). Published by the Royal Society of Chemistry

Open Access Article. Published on 27 April 2026. Downloaded on 6/17/2026 5:47:14 PM.
This article is licensed under a Creative Commons Attribution-NonCommercial 3.0 Unported Licence.

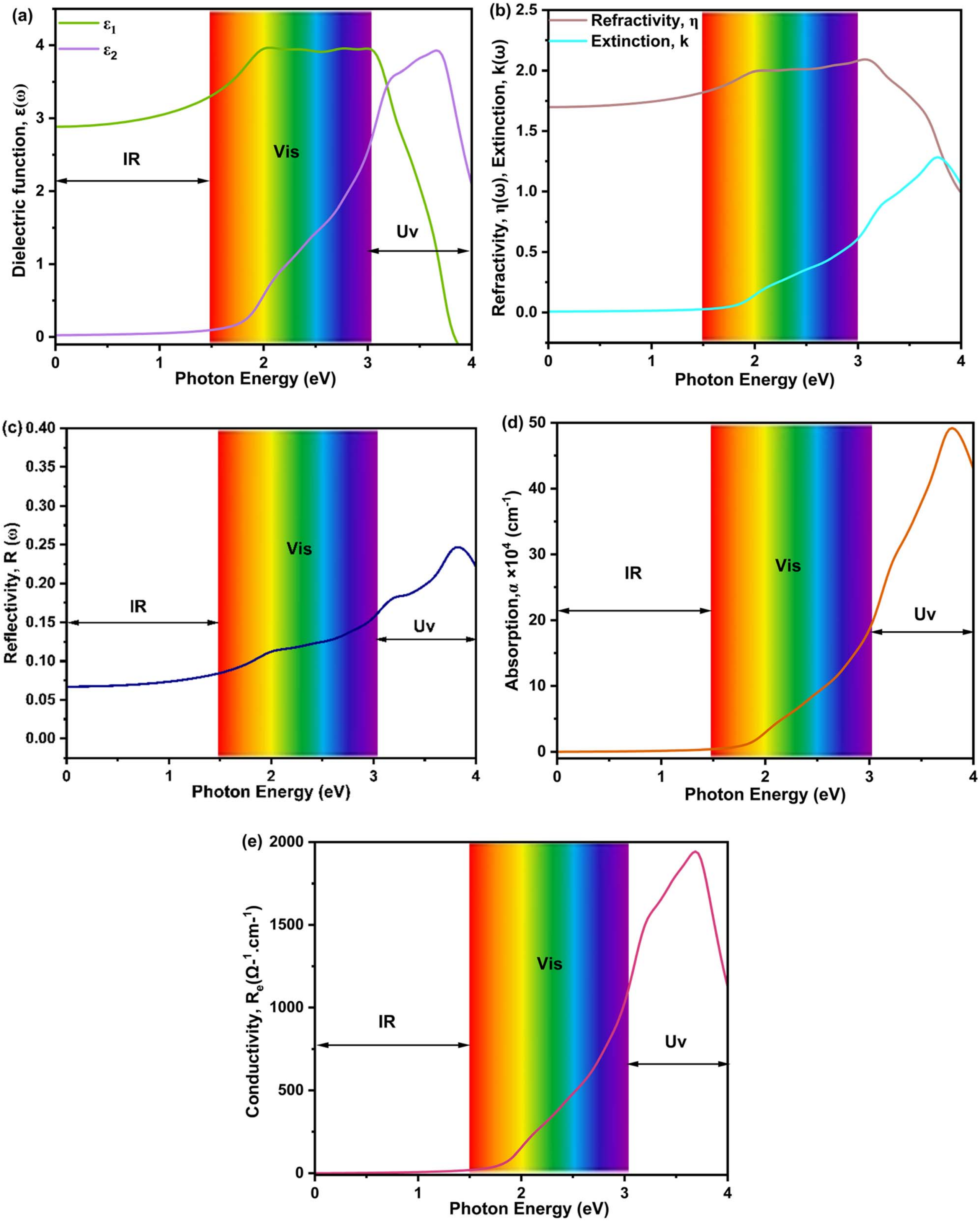

Fig. 6 The optical properties of the perovskite $Cs_2SnGeCl_6$ computed using TB-mBJ potential: (a) dielectric function, (b) refractivity and extinction function, (c) reflectivity function, (d) absorption coefficient, (e) conductivity.

due to the absence of a proper treatment of the exchange discontinuity. To overcome this limitation, TB-mBJ potential was employed, which provides an improved description of the exchange potential and has been demonstrated to produce bandgaps in much better agreement with experimental data for halide perovskites and related semiconductors, resulting in

© 2026 The Author(s). Published by the Royal Society of Chemistry

Open Access Article. Published on 27 April 2026. Downloaded on 6/17/2026 5:47:14 PM.
This article is licensed under a Creative Commons Attribution-NonCommercial 3.0 Unported Licence.

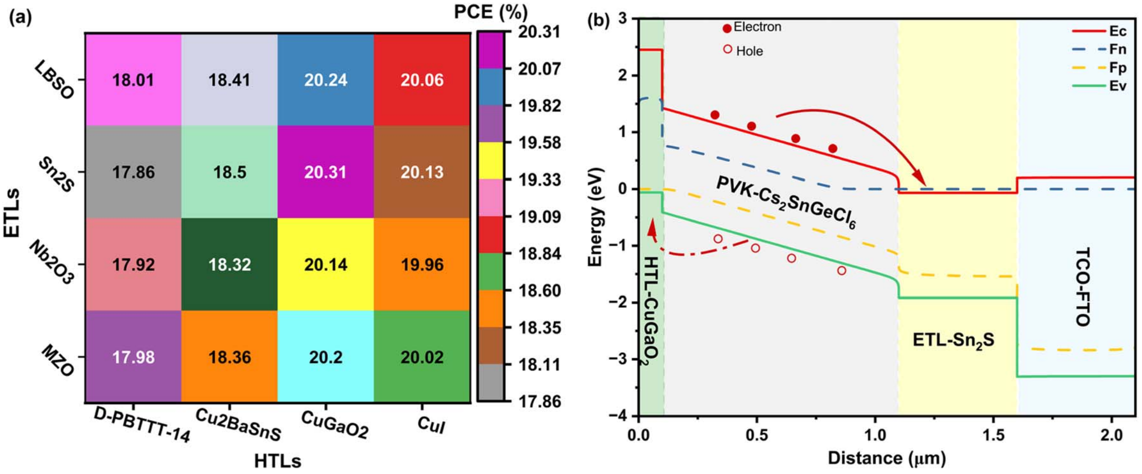

Fig. 7 (a) Heatmap of PCE for 16 configurations, (b) energy band diagram of best the configuration (FTO/SnS_2/$Cs_2SnGeCl_6$/$CuGaO_2$).

a larger direct bandgap of 1.837 eV (Γ). The preservation of the direct nature of the gap in both cases confirms the intrinsic optoelectronic character of the compound, while the TB-mBJ value is considered more realistic for assessing its suitability in photovoltaic and photonic applications. The total and partial density of states (DOS) of $Cs_2SnGeCl_6$ presented in the right side of Fig. 4, reveal that the valence band region (−4 eV to 0 eV) is mainly dominated by Cl orbitals, with additional hybridized contributions from Ge- and Sn states, confirming the halide-driven character of the valence band. In contrast, the conduction band region is primarily shaped by Sn orbitals, with Sn states making the largest contribution at the band edge, followed by Ge states, while Cl and Cs contribute only weakly. The absence of mid-gap states indicates electronic purity and reduced recombination losses. Additionally, while a difference in the total DOS is observed between two bands, the valence band has dispersions where the conduction band is relatively smooth (flats) and continuous, indicating moderate charge carrier mobility in valence bands compared to electron mobility,[49] confirming the suitability of $Cs_2SnGeCl_6$ as a promising p-type semiconductor for photovoltaic and optoelectronic devices.

The projected density of states (PDOS) of $Cs_2SnGeCl_6$ provides a detailed understanding of the atomic orbital contributions to the electronic structure near E_f as presented in Fig. 5. The valence band region below E_f is dominated primarily by the Cl-3p orbitals, which form the major contribution between −4 eV and 0 eV. This confirms that chlorine plays the leading role in defining the top of the valence band, consistent with the typical behavior of halide perovskites.[49] A secondary contribution in the same region arises from Sn-5s and Ge-4p orbitals, indicating weak hybridization with halide states.[50] In contrast, the conduction band region above the Fermi level is mainly governed by the B-site cations. The Sn-5p states represent the largest contribution near the conduction band minimum, followed by the Ge-4p orbitals, this indicates that electronic transitions across the bandgap primarily involve Cl-p → Sn-p/Ge-p states, and the Sn-5d and Ge-3d orbitals appear at slightly higher energies but still contribute to the conduction band profile. Otherwise, the Cs-5d and Cs-6s states lie far from the Fermi level, both in the deep valence and upper conduction regions, confirming their minimal influence on band-edge electronic behavior and their largely ionic/structural role in stabilizing the lattice.[8] The dominant Cl-p character at the valence band edge and Sn/Ge-p involvement in the conduction band edge support efficient optical absorption, while the relative orbital separation can facilitate favorable charge transport. These features reinforce the suitability of $Cs_2SnGeCl_6$ as a p-type semiconductor for optoelectronic and photovoltaic devices.[51]

The conduction band (CB) near the Fermi level exhibits limited dispersion, which implies a relatively high effective mass for electron carriers (m_e^*), as indicated by an examination of the band structure. The valence band (VB) has greater dispersion, indicating that holes possess a reduced effective mass (m_h^*). The effective mass of an electron or hole signifies the velocity at which it traverses the crystal lattice of a material. A reduced effective mass of the charge carrier may facilitate more mobility, hence augmenting electrical conductivity.[52]

$$m^* = \hbar^2 \times \left(\frac{\partial^2 E(k)}{\partial k^2}\right)^{-1} \tag{10}$$

where $m^*(k)$, $\hbar$, $E(k)$ and k are the effective mass, reduced Planck's constant, energy and wave vector, respectively (see Table 5).

The effective mass values for $Cs_2SnGeCl_6$ demonstrate that holes exhibit greater mobility than electrons, due to the latter having a larger effective mass. This behavior corresponds with that of p-type semiconductors, where electron transport predominates.[11] Furthermore, this behavior can be understood in light of recent theoretical insights reported by Fan *et al.*,[53] who demonstrated that carrier effective masses are strongly governed by crystal structure and orbital hybridization, localized electronic states and weak orbital overlap tend to produce flatter bands and higher electron effective masses, whereas stronger hybridization leads to more dispersive bands and lighter carriers. Although their study focuses on oxide

Open Access Article. Published on 27 April 2026. Downloaded on 6/17/2026 5:47:14 PM.
This article is licensed under a Creative Commons Attribution-NonCommercial 3.0 Unported Licence.

semiconductors, a similar mechanism can explain the relatively flat CB observed in $Cs_2SnGeCl_6$, suggesting limited orbital overlap in the conduction band states. Moreover, the effective mass influences the effective density of states in the valence band (N_V), which denotes the number of available states per unit volume near the band edges, and the conduction band (N_C). They are supplied by

$$N_c = 2\left(\frac{2\pi m_e^* k_B T}{\hbar^2}\right)^{3/2} \quad N_v = 2\left(\frac{2\pi m_h^* k_B T}{\hbar^2}\right)^{3/2} \tag{11}$$

where $\hbar$, k_B, and T are the Planck's constant, Boltzmann's constant, and temperature. The mobility of charge carriers ($\mu_{e/h}$) is associated with their relaxation time (τ) and effective mass (m^*) as expressed by the equation:

$$\mu_{e/h} = \frac{q\tau}{m^*} \tag{12}$$

where m^* is the carrier's effective mass (in kg), τ is the relaxation period (in seconds), $q = 1.602 \times 10^{-19}$ C is the elementary charge, and μ is the carrier mobility (in $cm^2\ V^{-1}\ s^{-1}$), Table 4 enlisted all electronic calculated parameters. The relaxation times for electrons and holes in analogous perovskite materials are typically 10^{-12} seconds, respectively.[54,55] Based on the optical properties, which will be elaborated in the subsequent section, we estimate the relaxation period of $Cs_2SnGeCl_6$ to be approximately 10^{-14} seconds. This indicates that charge carriers possess a brief lifespan and do not traverse significant distances prior to recombination.

3.3 Probing the optical properties of $Cs_2SnGeCl_6$ double halide perovskites

In photovoltaic devices, optical properties play a critical role in determining light absorption, exciton generation, and overall energy conversion efficiency. When electromagnetic radiation interacts with a material, it induces optical responses that directly influence both its electronic and photonic behavior. These responses are quantitatively described by the complex dielectric function $\varepsilon(\omega)$, which provides a comprehensive representation of the material's optical characteristics. The subsequent expression delineates the complex dielectric function $\varepsilon(\omega)$ about angular frequency:

$$\varepsilon(\omega) = \varepsilon_1(\omega) + i\varepsilon_2(\omega) \tag{13}$$

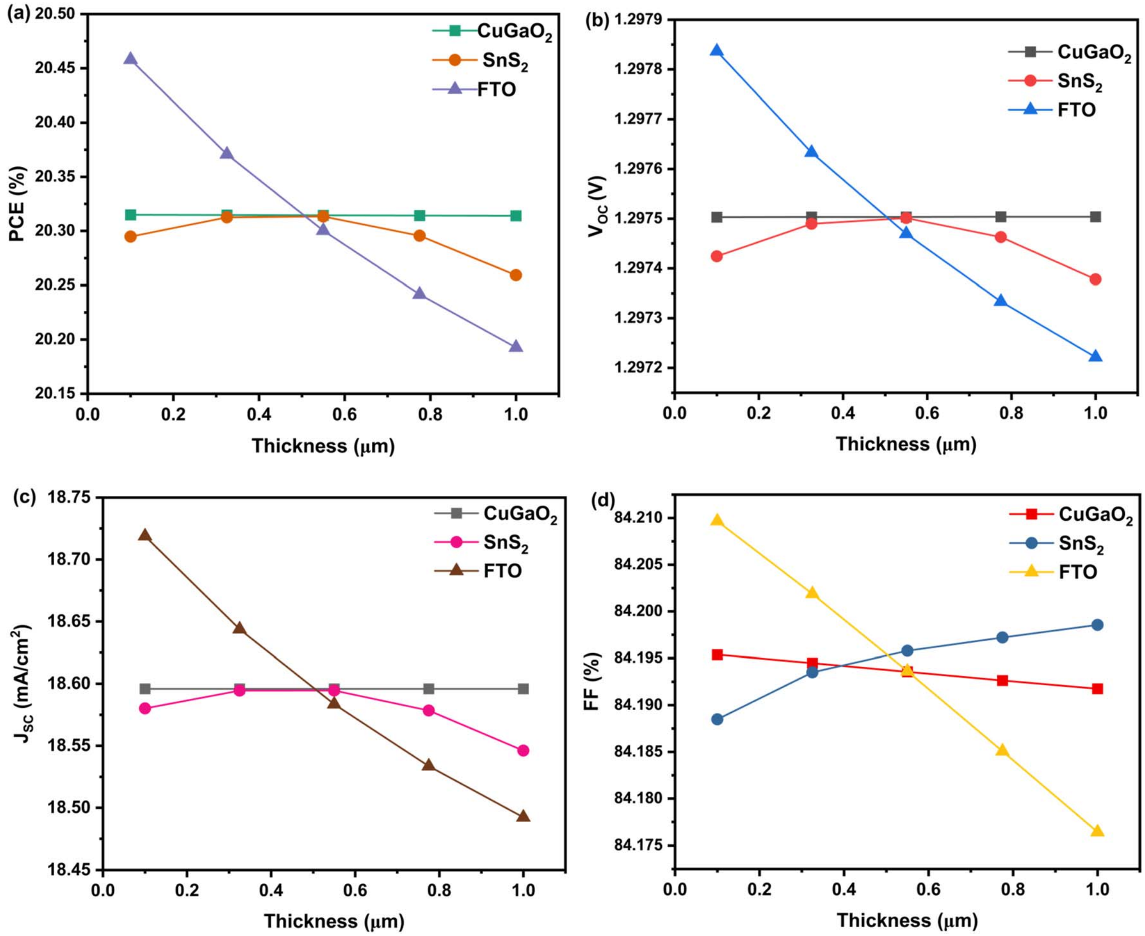

Fig. 8 Impact of thickness of TCO (FTO), HTL ($CuGaO_2$), and ETL (SnS_2) on (a) PCE, (b) J_{SC}, (c) V_{OC}, and (d) FF.

Open Access Article. Published on 27 April 2026. Downloaded on 6/17/2026 5:47:14 PM.
This article is licensed under a Creative Commons Attribution-NonCommercial 3.0 Unported Licence.

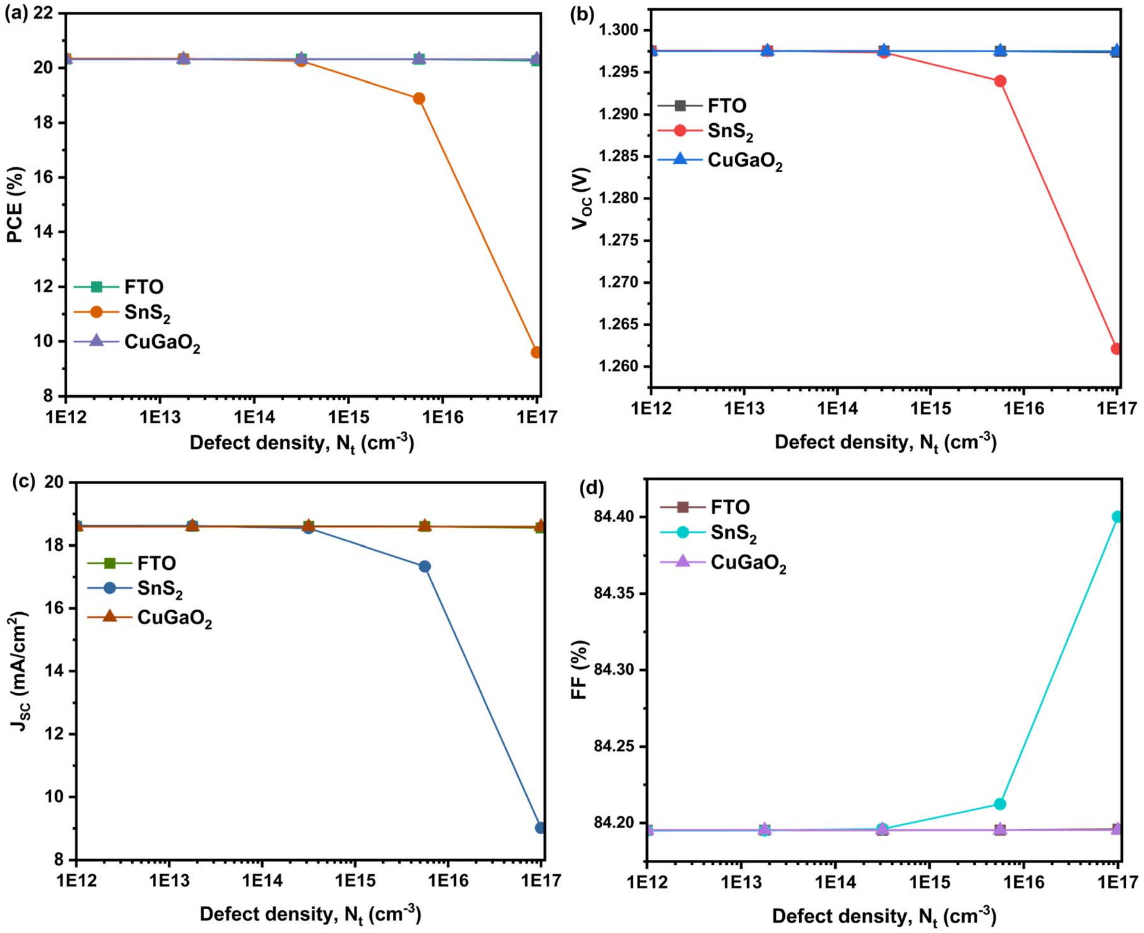

Fig. 9 Impact of defect density, N_t of TCO (FTO), HTL ($CuGaO_2$), and ETL (SnS_2) on (a) PCE, (b) J_{SC}, (c) V_{OC}, and (d) FF.

The real part of the dielectric function, $\varepsilon_1(\omega)$, is associated with the material's ability to store electromagnetic energy through polarization and directly influences key optical phenomena such as refraction, reflection, and the propagation speed of light within the medium. Since it is linked to the refractive index, $\varepsilon_1(\omega)$ provides insight into how the material responds to an external electric field without energy loss. In contrast, the imaginary part, $\varepsilon_2(\omega)$, describes the absorption and dissipation of electromagnetic energy inside the material. It governs the absorption coefficient and thus determines how effectively the material absorbs incident light at different photon energies or frequencies. Together, $\varepsilon_1(\omega)$ and $\varepsilon_2(\omega)$ provide a complete description of the optical response relevant to photovoltaic applications. Using eqn (13), several key optical constants were derived, including refractive index $\eta(\omega)$, extinction coefficient $k(\omega)$, reflectivity $R(\omega)$, absorption coefficient $\alpha(\omega)$, and optical conductivity $\sigma(\omega)$

$$\begin{aligned}\eta(\omega) &= \left(\sqrt{{\varepsilon_1}^2(\omega)+{\varepsilon_2}^2(\omega)}+\varepsilon_1(\omega)\right)^{1/2}\Big/\sqrt{2}\\ k(\omega) &= \left(\sqrt{{\varepsilon_1}^2(\omega)+{\varepsilon_2}^2(\omega)}-\varepsilon_1(\omega)\right)^{1/2}\Big/\sqrt{2}\end{aligned} \tag{14}$$

$$R(\omega) = \left|\frac{\varepsilon(\omega)^{1/2}-1}{\varepsilon(\omega)^{1/2}+1}\right|^2 \tag{15}$$

$$\alpha(k) = \sqrt{2}\omega\left(\sqrt{{\varepsilon_1}^2(\omega)+{\varepsilon_2}^2(\omega)}-\varepsilon_1(\omega)\right)^{1/2} \tag{16}$$

$$\sigma(\omega) = \frac{-i\omega\varepsilon(\omega)}{4\pi} \tag{17}$$

The optical response of $Cs_2SnGeCl_6$ was analyzed through several parameters across the photon energy range covering the visible (Vis) region. The Fig. 6(a) presents the dielectric function, where the real part of the dielectric function $\varepsilon_1(\omega)$ increases gradually and reaches its maximum within the visible range, indicating strong polarization ability and efficient interaction with incoming light. The imaginary part $\varepsilon_2(\omega)$ starts rising near the fundamental absorption edge, confirming the onset of interband transitions consistent with the calculated bandgap. The behavior of the refractive index $\eta(\omega)$ follows that of $\varepsilon_1(\omega)$, showing elevated values in the visible region (see Fig. 6(b)), which is advantageous for slowing and trapping incident light in photovoltaic absorbers. The extinction coefficient $k(\omega)$ begins to increase shortly after the absorption onset,

© 2026 The Author(s). Published by the Royal Society of Chemistry

Open Access Article. Published on 27 April 2026. Downloaded on 6/17/2026 5:47:14 PM.
This article is licensed under a Creative Commons Attribution-NonCommercial 3.0 Unported Licence.

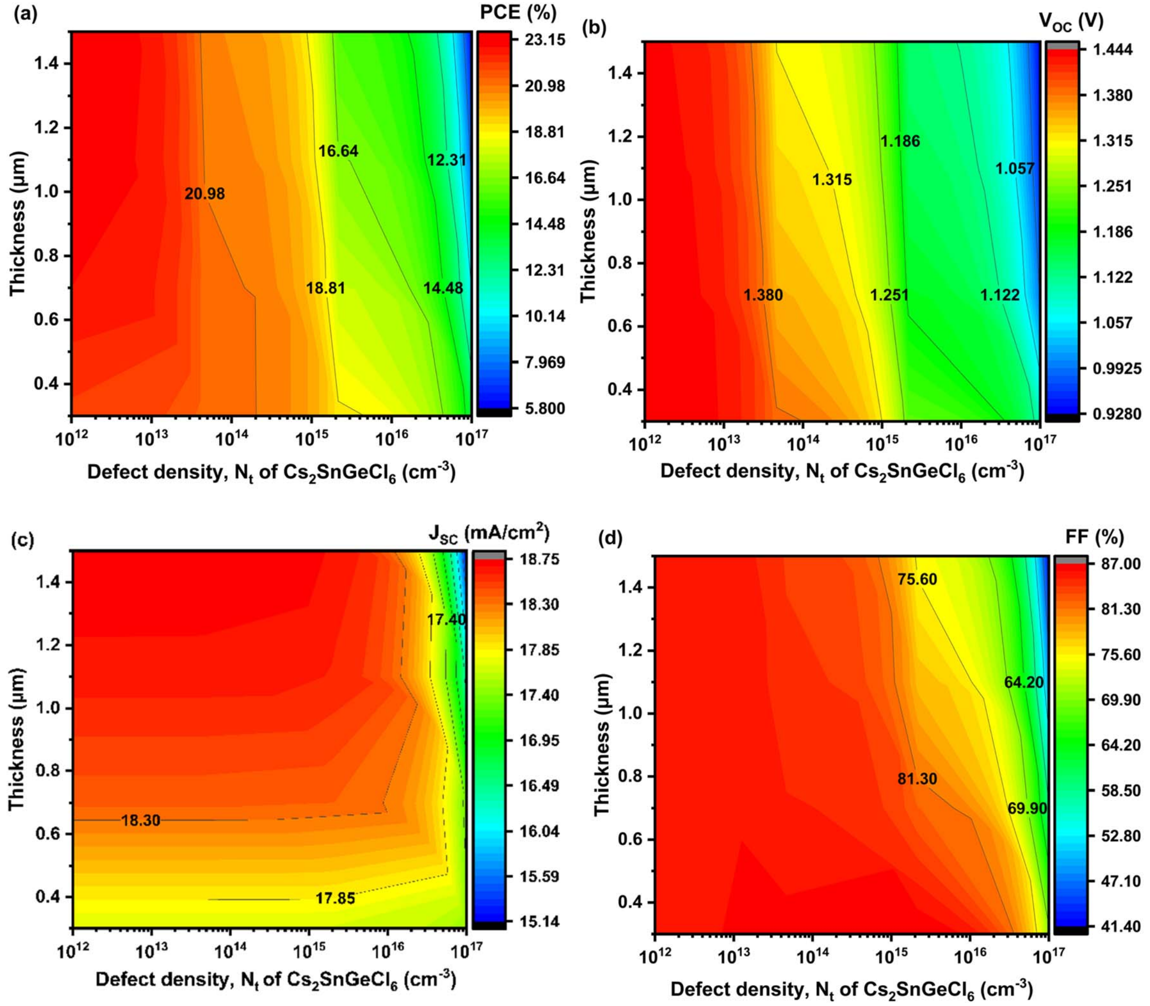

Fig. 10 Impact of thickness and defect density of PVK ($Cs_2SnGeCl_6$) in contour mapping on (a) PCE, (b) J_{SC}, (c) V_{OC}, and (d) FF.

reflecting enhanced photon attenuation and efficient light-matter coupling. The reflectivity spectrum of $Cs_2SnGeCl_6$ presented in Fig. 6(c), shows a weak response at low photon energies, consistent with its semiconducting nature and absence of metallic character. As the photon energy increases, the reflectivity gradually rises, but within the visible range it remains relatively modest, typically below ∼25–30%, which is advantageous for photovoltaic applications since it ensures that most of the incident light is absorbed rather than reflected. This low reflectivity across the visible spectrum highlights the material's suitability as an efficient solar absorber. At higher photon energies, beyond the visible region, the reflectivity increases more sharply, reaching stronger values due to enhanced inter-band electronic transitions. Moreover, the absorption coefficient $\alpha(\omega)$ is presented in Fig. 6(d), shows a rapid rise in the visible range (to 2×10^5 cm^{-1}), demonstrating the material's strong capability to absorb solar radiation, which is essential for photovoltaic and optoelectronic applications. Fig. 6(e) illustrates that the optical conductivity $\sigma(\omega)$ closely aligns with the absorption coefficient $\alpha(\omega)$, hence affirming robust photon–matter interaction. Collectively, these spectra confirm that $Cs_2SnGeCl_6$ exhibits desirable optical behavior across the visible region, supporting its potential use as an efficient light-harvesting material in solar cell architectures. In the subsequent section, $Cs_2SnGeCl_6$ is employed for the first time as the absorber layer in a perovskite solar cell structure and modeled using SCAPS-1D. The objective is to simulate and analyze the electrical and optical behavior of the $Cs_2SnGeCl_6$-based device, followed by performance optimization. The findings aim to provide a preliminary prototype framework that could serve as a reference for future experimental fabrication efforts.

3.4 Simulation and design of $Cs_2SnGeCl_6$-based chloride perovskite solar cells

To translate the DFT-derived material parameters into device-level performance, sixteen $Cs_2SnGeCl_6$-based perovskite solar cell structures were simulated in SCAPS-1D using four different ETLs and four HTLs as shown in Table 1. The resulting power conversion efficiencies (PCEs), displayed as a heatmap as presented in Fig. 7(a), reveal a clear dependence of device behavior on the interfacial layer combinations. The efficiencies span from 17.86% to 20.31%, which is significant for double-halide,

Open Access Article. Published on 27 April 2026. Downloaded on 6/17/2026 5:47:14 PM.
This article is licensed under a Creative Commons Attribution-NonCommercial 3.0 Unported Licence.

lead-free perovskite absorbers. The highest efficiencies, all above 20%, are concentrated in configurations employing high-quality hole-transport layers such as $CuGaO_2$, in combination with suitable ETLs. These devices reach PCE values of 20.31%, 20.24%, 20.20%, 20.14%, 20.13%, 20.06%, and 20.02%, demonstrating efficient charge extraction, favorable interfacial energetics, and reduced recombination losses at the absorber/HTL interface. In contrast, the lower-performing devices, ranging from 17.86% to 18.01%, are predominantly associated with HTLs such as D-PBTTT-14 showing less optimal ETL/HTL alignments. These combinations experience more pronounced interfacial recombination and carrier transport limitations, which restrict the achievable PCE. Cu_2BaSnS_4 and CuI HTLs exhibit moderate results, demonstrating slight alignment with ETLs. The heatmap clearly demonstrates that the photovoltaic performance of $Cs_2SnGeCl_6$-based devices is highly sensitive to the selection of both charge transport layers. Among all simulated architectures, the FTO/SnS_2/$Cs_2SnGeCl_6$/$CuGaO_2$ configuration delivers the most efficient performance, achieving a PCE of 20.31%, along with a V_{OC} of 1.305 V, J_{SC} of 18.60 mA cm^{-2}, and a FF of 83.68%. The superior output of this device can be directly linked to its favorable band alignment (Fig. 7(b)). At the ETL/absorber interface (SnS_2/$Cs_2SnGeCl_6$), a small spike-like conduction band offset is formed, which assists electron transfer while minimizing interfacial recombination.[56] Meanwhile, at the absorber/HTL interface ($Cs_2SnGeCl_6$/$CuGaO_2$), the absence of a cliff ensures smooth hole extraction without creating recombination sites. This balanced energy-level alignment enables efficient charge separation and transport in both directions, explaining the exceptional overall device performance.

This section explores how varying the thicknesses of the transport and contact layers influences the performance of $Cs_2SnGeCl_6$-based solar cells. The $CuGaO_2$ HTL, SnS_2 ETL, and FTO TCO were each adjusted from 0.1 to 1 μm, as presented in Fig. 8. Across this range, the photovoltaic parameters remain largely unchanged, with the exception of the power conversion efficiency. The PCE increases only slightly, from 20.18% to 20.50%, and this minor improvement is attributed solely to changes in the FTO (TCO) thickness (lowest thickness 0.1 μm). In contrast, modifying the thickness of SnS_2 (ETL) or $CuGaO_2$ (HTL) produces no meaningful impact on device output. These findings suggest that tuning the TCO thickness can marginally enhance carrier collection and mitigate interfacial recombination, while altering the ETL and HTL thickness mostly adds to series resistance without contributing to overall efficiency.

Defect density (N_t) is another key parameter that can influence photovoltaic performance. In this section, we assess the effect of

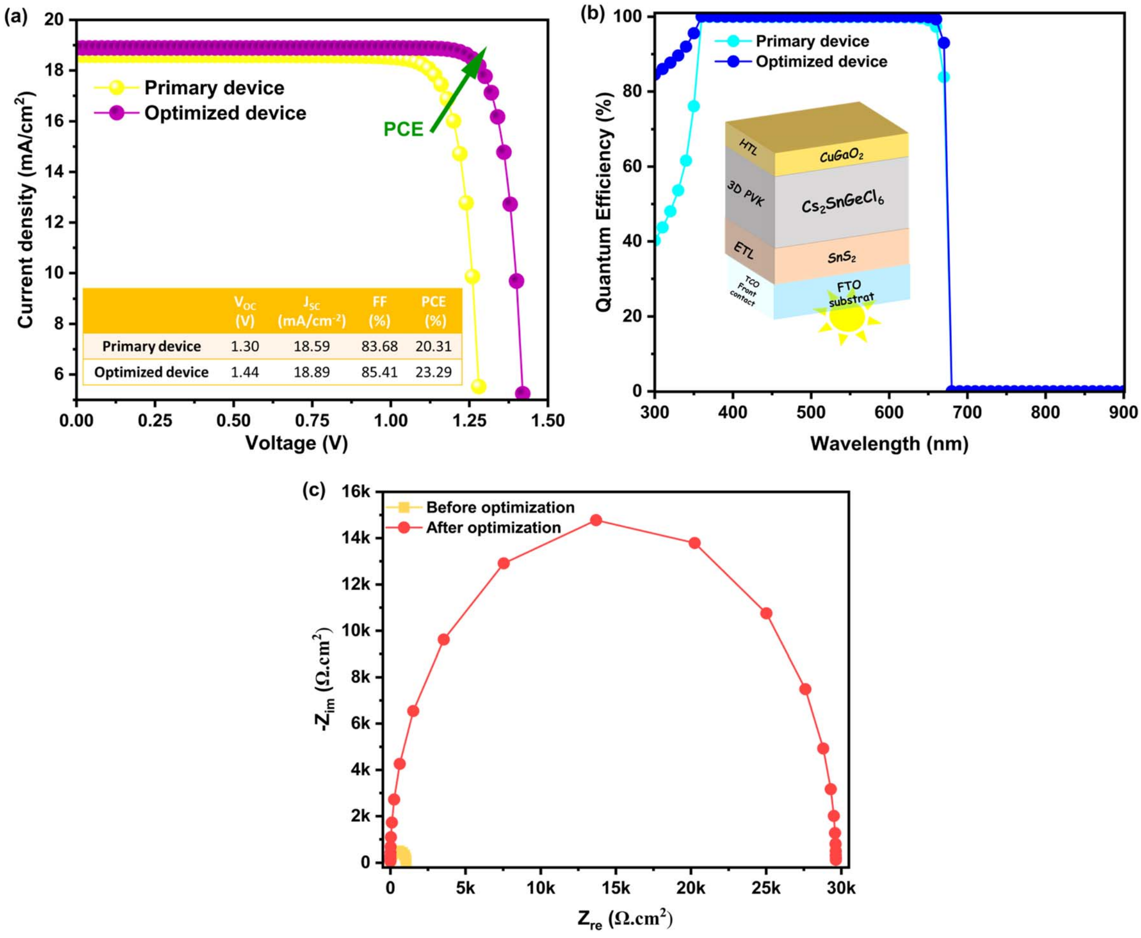

	V_{OC} (V)	J_{SC} (mA/cm^{-2})	FF (%)	PCE (%)
Primary device	1.30	18.59	83.68	20.31
Optimized device	1.44	18.89	85.41	23.29

Fig. 11 *J–V* curve (a), QE (b), and Nyquist plot (c) for device before and after optimization.

Open Access Article. Published on 27 April 2026. Downloaded on 6/17/2026 5:47:14 PM.
This article is licensed under a Creative Commons Attribution-NonCommercial 3.0 Unported Licence.

Table 6 Table of comparison between our device and reports from literature

Device configuration	V_{OC} (V)	J_{SC} (mA cm^{-2})	FF (%)	PCE (%)	Ref.
ITO/SnO_2/hydrogenated-$Cs_2AgBiBr_6$/spiro-OMeTAD/Au	0.92	11.4	0.609	6.37	Exp[58]
FTO/CZTS/$Cs_2BiAgBr_6$/ZnOS/Au	1.25	16.48	90.60	18.71	Sim[59]
ZnS/Cs_2MgGeI_6/$CuAlO_2$	1.04	27.14	81.72	23.13	Sim[6]
FTO/SnS_2/$Cs_2SnGeCl_6$/$CuGaO_2$	**1.44**	**18.89**	**85.41**	**23.29**	**This work**

N_t in the TCO, HTL, and ETL layers by varying it from 10^{12} to 10^{17} cm^{-3}, as shown in Fig. 9. The results show that increasing the defect density in the TCO (FTO) and HTL ($CuGaO_2$) has a negligible impact on device performance, indicating good defect tolerance in these layers. In contrast, defects in the ETL (SnS_2) significantly degrade the photovoltaic parameters, with noticeable reductions in PCE, V_{OC}, and J_{SC} as N_t increases. Interestingly, FF is the only parameter that improves with higher defect density in the ETL. This increase may be related to the reduction of series resistance or altered charge extraction dynamics at the ETL/absorber interface, which partially compensates for the recombination losses caused by defect states.[57] However, the overall impact of higher N_t in the ETL remains detrimental to device efficiency, highlighting the importance of minimizing defects specifically in this layer.

Among all layers in a photovoltaic device, the absorber plays the most crucial role, as it governs both light harvesting and charge carrier generation. To assess its impact on device performance, the thickness and defect density (N_t) of the $Cs_2SnGeCl_6$ absorber were systematically varied. The absorber thickness was adjusted from 0.3 to 1.5 μm, while the defect density was modified from 10^{12} to 10^{17} cm^{-3}. As illustrated by the contour plot in Fig. 10, the best photovoltaic performance is achieved when the absorber thickness is set to higher thickness of 1.5 μm and the defect density is kept at lowest value of 10^{12} cm^{-3}. The observed trend indicates that maintaining a low defect density and avoiding excessive absorber thickness are both critical to reducing non-radiative recombination and enhancing carrier extraction, which collectively support higher 1.44 V of V_{OC}, 18.75 mA cm^{-2} of J_{SC}, 85.82% of FF, and ultimately 23.11% of PCE. This emphasizes that achieving high crystallinity and carefully controlling absorber thickness are essential requirements for maximizing overall device performance.

We have derived the optimum parameters for ETL, HTL, TCO, and absorber layer regarding thickness and defect density to enhance the overall photovoltaic characteristics of our device depicted in the inset of Fig. 11. The overall device performance was significantly improved, which illustrated the importance of maintaining a balance between layer thicknesses and defect passivation in order to optimize efficiency, where the PCE increasing from 20.31% to 23.29%, as presented in the J–V curve in Fig. 11(a) and the inset table where other photovoltaic parameters were improved: V_{OC} increased from 1.30 to 1.44 V, J_{SC} from 18.59 to 18.89 mA cm^{-2}, and FF from 83.68% to 85.41%. The external quantum efficiency (EQE) spectra of the device after optimization reveal a clear enhancement in photocarrier generation across the visible range (300–500 nm) as presented Fig. 11(b), demonstrating a significant improvement in carrier collection and reduced recombination losses. The Nyquist plots (Fig. 11(c)) demonstrate a significant increase in the semicircle diameter for the optimized device relative to the original device. This expansion signifies elevated charge-transfer resistance at the perovskite/HTL interface, suggesting enhanced hole transport and reduced interfacial recombination. Given that recombination losses at interfaces frequently constrain the performance of perovskite solar cells, the enhanced Nyquist response robustly corroborates the efficacy of our optimization technique, as reported in earlier reports.[56]

As far as we know, this is the first report to use $Cs_2SnGeCl_6$ as an absorber material in a perovskite solar cell. Table 6 shows how well the proposed FTO/SnS_2/$Cs_2SnGeCl_6$/$CuGaO_2$ device works as a solar cell compared to other double-halide perovskite solar cells that have been reported. The optimized $Cs_2SnGeCl_6$-based structure attains remarkable photovoltaic parameters that surpass those of the majority of previously experimental and simulated systems.

4. Conclusion

The structural, mechanical, optoelectronic, and vibrational properties of the lead-free double perovskite $Cs_2SnGeCl_6$ were comprehensively explored through advanced first-principles calculations using WIEN2k with GGA-PBE and TB-mBJ functionals. Stability assessments-including the Goldschmidt tolerance factor, formation energy, elastic constants, and phonon dispersion confirm that $Cs_2SnGeCl_6$ is structurally, thermodynamically, and mechanically resilient, supporting its feasibility for real-world applications. The direct bandgaps obtained (0.890 eV with GGA and 1.837 eV with TB-mBJ) demonstrate favorable optical transitions across the visible and near-infrared regions, further reinforced by strong absorption and promising carrier transport characteristics. To translate these electronic insights into device-scale predictions, DFT-derived parameters were incorporated into SCAPS-1D simulations for the first time. The optimized n–i–p configuration, FTO/SnS_2/$Cs_2SnGeCl_6$/$CuGaO_2$, achieved a notable power conversion efficiency of 23.29%, underscoring its promise for high-performance, lead-free perovskite solar cells. Overall, this work establishes a strong theoretical foundation for the experimental synthesis and technological deployment of $Cs_2SnGeCl_6$. It is a versatile candidate for the next-generation solar-energy conversion due to its combined photovoltaic and photocatalytic capabilities.

Conflicts of interest

The authors declare no conflict of interest.

Open Access Article. Published on 27 April 2026. Downloaded on 6/17/2026 5:47:14 PM.
This article is licensed under a Creative Commons Attribution-NonCommercial 3.0 Unported Licence.

Data availability

All data that support the findings of this study are included with the article.

Acknowledgements

The Deanship of Scientific Research, Vice Presidency supported this research for Graduate Studies and Scientific Research, King Faisal University, Saudi Arabia. [Grant No. KFU261683].

References

1 M. W. Alam, *Breaking Boundaries: Pioneering Sustainable Solutions through Materials and Technology*, Springer Nature Singapore, Singapore, 2025.
2 M. Y. Khan, M. A. Jehangir, N. Israr, A. Hassan, U. Younis, J. Khan, M. Khan, A. Khan and A. Al Souwaileh, *Phys. B*, 2025, **707**, 417150.
3 A. I. Shimul, B. Chandra Biswas, A. Ghosh, H. A. Alrafai and A. A. Hassan, *Sol. Energy Mater. Sol. Cells*, 2025, **293**, 113838.
4 A. I. Shimul, A. T. M. S. Islam, A. Ghosh, M. M. Hossain, S. A. Dipa and R. J. Ramalingam, *Comput. Mater. Sci.*, 2025, **250**, 113701.
5 NREL, NREL, Best Research-Cell Efficiencies, 2024, https://www.nrel.gov/pv/cell-efficiency.html.
6 A. N. Khan, N. U. Khan, M. Kaleem, M. Tanzeel, A. Nasir, A. Hosen, A. Akremi and I. Boukhris, *Solid State Sci.*, 2025, **168**, 108049.
7 A. I. Shimul, A. Ghosh, S. R. Sarker and H. A. Alturaifi, *RSC Adv.*, 2025, **15**, 7663–7681.
8 A. I. Shimul, A. Ghosh, M. F. Ahmed, A. S. Mugdho, Z. Hasan, N. S. Awwad and H. A. Ibrahium, *Langmuir*, 2025, **41**, 13655–13674.
9 A. I. Shimul, M. M. Haque, A. Ghosh, M. A. U. Sunny, S. O. Aljazzar, J. Y. Al-Humaidi and Y. E. Mukhrish, *J. Inorg. Organomet. Polym. Mater.*, 2025, DOI: 10.1007/s10904-025-03629-3.
10 S. Al-Qaisi, N. Iram, N. Sfina, A. Boutramine, H. R. Jappor, A. H. Alfaifi, H. S. Alzahrani, H. Rached, M. A. Ali and G. Murtaza, *Phys. B*, 2025, **710**, 417239.
11 A. N. Khan, M. Kaleem, N. U. Khan, A. Nasir, A. Khan and M. Z. Abbasi, *Sol. Energy Mater. Sol. Cells*, 2026, **294**, 113922.
12 A. Boutramine, S. Al-Qaisi, S. Samah, A. K. Alqorashi, T. A. Alrebdi, M. Ezzeldien and M. F. Rahman, *J. Inorg. Organomet. Polym. Mater.*, 2024, **34**, 4133–4145.
13 Z. Xiao, W. Meng, J. Wang and Y. Yan, *ChemSusChem*, 2016, **9**, 2628–2633.
14 C. Wu, B. Du, W. Luo, Y. Liu, T. Li, D. Wang, X. Guo, H. Ting, Z. Fang, S. Wang, Z. Chen, Y. Chen and L. Xiao, *Adv. Opt. Mater.*, 2018, **6**, DOI: 10.1002/adom.201800811.
15 H. Murtaza, Q. Ain, J. Munir, H. M. Ghaithan, M. Ali, A. A. Ali Ahmed and S. M. Saif, *J. Phys. Chem. Solids*, 2024, **190**, 111934.
16 W. Zheng, X. Gan, D. Du, Y. Wang, S. Dai, L. Guo and H. Liu, *J. Wuhan Univ. Technol., Mater. Sci. Ed.*, 2023, **38**, 520–529.
17 P. Blaha, K. Schwarz, P. Sorantin and S. B. Trickey, *Comput. Phys. Commun.*, 1990, **59**, 399–415.
18 P. Blaha, K. Schwarz, F. Tran, R. Laskowski, G. K. H. Madsen and L. D. Marks, *J. Chem. Phys.*, 2020, **152**(7), DOI: 10.1063/1.5143061.
19 J. P. Perdew, K. Burke and M. Ernzerhof, *Phys. Rev. Lett.*, 1996, **77**, 3865–3868.
20 D. Koller, F. Tran and P. Blaha, *Phys. Rev. B: Condens. Matter Mater. Phys.*, 2012, **85**, 155109.
21 B. Traoré, G. Bouder, W. Lafargue-Dit-Hauret, X. Rocquefelte, C. Katan, F. Tran and M. Kepenekian, *Phys. Rev. B*, 2019, **99**, 035139.
22 H. J. Monkhorst and J. D. Pack, *Phys. Rev. B*, 1976, **13**, 5188–5192.
23 M. Burgelman, P. Nollet and S. Degrave, *Thin Solid Films*, 2000, **361**, 527–532.
24 E. Dunlop, F. Fabero, G. Friesen, W. Herrmann, J. Hohl-Ebinger, H.-D. Mohring, H. Mullejans, A. Virtuani, W. Warta, W. Zaaiman, S. Zamini and N. Taylor, Energy Conversion & Hydrogen, *Guidelines for PV Power Measurement in Industry*, 2010.
25 S. Karthick, J. Bouclé and S. Velumani, *Sol. Energy*, 2021, **218**, 157–168.
26 A. Bouich, J. C. Torres, H. Chfii, J. Marí-Guaita, Y. H. Khattak, F. Baig, B. M. Soucase and P. Palacios, *Sol. Energy*, 2023, **250**, 18–32.
27 N. K. Singh and A. Agarwal, *Energy Sources, Part A*, 2023, **45**, 3087–3106.
28 E. N. Vincent Mercy, D. Srinivasan and L. Marasamy, *ACS Omega*, 2024, **4**, 4359–4376.
29 N. Rono, A. E. Merad, J. K. Kibet, B. S. Martincigh and V. O. Nyamori, *Energy Technol.*, 2021, **9**, 2100859.
30 P. Saha, S. Singh and S. Bhattacharya, *IEEE Trans. Electron Devices*, 2023, **70**, 1095–1101.
31 K. Shivesh, I. Alam, A. K. Kushwaha, M. Kumar and S. V. Singh, *Int. J. Energy Res.*, 2022, **46**, 6045–6064.
32 F. Kherrat, L. Dehimi, H. Bencherif, M. M. A. Moon, M. K. Hossain, N. A. Sonmez, T. Ataser, Z. Messai and S. Özçelik, *Micro Nanostruct.*, 2023, **183**, DOI: 10.1016/j.micrna.2023.207676.
33 F. BIRCH, *J. Geophys. Res.*, 1978, **83**, 1257–1268.
34 L. Dahane and H. Ez-Zahraouy, *Int. J. Hydrogen Energy*, 2025, **145**, 589–600.
35 D. Bharath Raja, R. Vidya and K. Shanmuga Sundaram, *Sol. Energy*, 2022, **245**, 353–364.
36 C. J. Bartel, C. Sutton, B. R. Goldsmith, R. Ouyang, C. B. Musgrave, L. M. Ghiringhelli and M. Scheffler, *Sci. Adv.*, 2019, **5**, 1–9.
37 I. N. Flerov, M. V. Gorev, K. S. Aleksandrov, A. Tressaud, J. Grannec and M. Couzi, *Mater. Sci. Eng., R*, 1998, **24**, 81–151.
38 V. M. Goldschmitdt, *Naturwissenschaften*, 1926, **14**, 477–485.
39 C. Gao, J. Zhu, S. Ye, M. Li, H. Wang and J. He, *J. Eur. Ceram. Soc.*, 2025, **45**, 116878.
40 K. W. Guji, T. A. Geleta, N. Bouri and V. J. Ramirez Rivera, *Nanoscale Adv.*, 2024, **6**, 4479–4491.

Open Access Article. Published on 27 April 2026. Downloaded on 6/17/2026 5:47:14 PM. This article is licensed under a Creative Commons Attribution-NonCommercial 3.0 Unported Licence.

41 M. Jamal, M. Bilal, I. Ahmad and S. Jalali-Asadabadi, *J. Alloys Compd.*, 2018, **735**, 569–579.

42 O. L. Anderson, *J. Phys. Chem. Solids*, 1963, **24**, 909–917.

43 R. Hill, *Proc. Phys. Soc., London, Sect. A*, 1952, **65**, 349–354.

44 R. Ali, Z. G. Zhu, Q. B. Yan, Q. R. Zheng, G. Su, A. Laref, C. S. Saraj and C. Guo, *ACS Appl. Mater. Interfaces*, 2020, **12**, 49636–49647.

45 S. Rabhi, A. N. Khan, O. Chinoune, R. Charif, N. Bouri, S. Al-Qaisi, S. Sadaf, A. BaQais and M. W. Alam, *Phys. Chem. Chem. Phys.*, 2025, **27**, 13490–13507.

46 A. Boutramine, S. Al-Qaisi, N. Sfina, L. A. Lamine, H. Chaib, M. Archi, O. Alsalmi and S. Rabhi, *Surf. Interfaces*, 2025, **72**, 107269.

47 M. E. Fine, L. D. Brown and H. L. Marcus, *Scr. Metall.*, 1984, **18**, 951–956.

48 C. Zener, *Phys. Rev.*, 1936, **49**, 122–127.

49 A. N. Khan, S. Rabhi, N. U. Khan, S. A. Ansari, S. Sadaf and M. W. Alam, *Ceram. Int.*, 2025, **51**, 59579–59589.

50 L. Benahmedi, A. Besbes, R. Djelti, S. Moulebhar, A. Aissani and S. Bendehiba, *Sol. Energy*, 2025, **300**, 113860.

51 A. I. Shimul, S. R. Sarker, A. Ghosh, M. Moumita, N. L. Dey, K. U. Apu and N. S. Awwad, *New J. Chem.*, 2025, **49**, 14300–14321.

52 M. Y. Khan, M. A. Jehangir, I. E. Lee, Q. Wali, T. Usman, L. Xiaojie and A. Al Souwaileh, *Chem. Phys. Impact*, 2025, **11**, 10.

53 Q. Fan, R. Zhao, W. Zhang, Y. Song, M. Sun and U. Schwingenschlögl, *Phys. Chem. Chem. Phys.*, 2022, **24**, 7045–7049.

54 R. L. Milot, R. J. Sutton, G. E. Eperon, A. A. Haghighirad, J. Martinez Hardigree, L. Miranda, H. J. Snaith, M. B. Johnston and L. M. Herz, *Nano Lett.*, 2016, **16**, 7001–7007.

55 G. Folpini, L. Gatto, D. Cortecchia, M. Devetta, G. Crippa, C. Vozzi, S. Stagira, A. Petrozza and E. Cinquanta, *J. Chem. Phys.*, 2020, **152**, DOI: 10.1063/5.0008608.

56 T. Minemoto and M. Murata, *Sol. Energy Mater. Sol. Cells*, 2015, **133**, 8–14.

57 N. Bouri, T. A. Geleta, K. W. Guji, A. Hammad, S. Rabhi and K. Nouneh, *J. Phys. Chem. Solids*, 2025, **207**, 112972.

58 F. Ji, G. Boschloo, F. Wang and F. Gao, *Sol. RRL*, 2023, **7**(6), DOI: 10.1002/solr.202201112.

59 S. Ullah, T. Alshahrani, F. Khan and F. Rasheed J, *Mater. Today Commun.*, 2024, **38**, 108514.

© 2026 The Author(s). Published by the Royal Society of Chemistry